Korean J. Chem. Eng., 37(3), 423-433 (2020)
DOI: 10.1007/s11814-019-0456-y

pISSN: 0256-1115
eISSN: 1975-7220

A detailed numerical study on the evolution of droplet size distribution of dibutyl phthalate in a laminar flow diffusion chamber

Feng Jia*, Zi-Yi Li, David Y. H. Pui***,****, and Chuen-Jinn Tsai*,†**

*Institute of Environmental Engineering, National Chiao Tung University, Hsinchu 300, Taiwan
**School of Energy and Environmental Engineering, University of Science and Technology Beijing, Beijing 100083, China
***Mechanical Engineering Department, University of Minnesota, Minneapolis, MN 55455, USA
****School of Science and Engineering, The Chinese University of Hong Kong, Shenzhen, Guangdong 518172, China
(*Received 25 September 2019 • accepted 7 December 2019*)

Abstract−A numerical model was used to study the homogeneous nucleation process of dibutyl phthalate (DBP) vapor in a laminar flow diffusion chamber (LFDC); the spatial and temporal evolution of DBP droplet size distribution was governed by the population balance equation (PBE). In the PBE, the nucleation rate was calculated by the self-consistent correction nucleation theory (SCCNT), droplet coagulation, vapor and droplet deposition losses were considered. The simulation results showed that the nucleation rate predicted by the SCCNT improved the underestimation of that predicted by the classical nucleation theory. Due to vapor deposition before nucleation and droplet deposition after nucleation on the wall, the DBP mass loss was severe, accounting for about 86.3% of the total inlet vapor mass, and the droplet size distribution shifted towards larger diameters. The simulation results agreed well with the experimental data in terms of the droplet size distribution and average number concentration at the outlet of the LFDC because of the detailed droplet dynamic, transport and deposition mechanisms treated in this model. Based on this model, the number of molecules in the critical cluster was calculated using the first nucleation theorem and found to be larger about 50% than that calculated using the Gibbs-Thompson equation.

Keywords: Homogeneous Nucleation, Dibutyl Phthalate, Laminar Flow Diffusion Chamber, Coagulation, Vapor and Droplet Deposition, OpenFOAM®

INTRODUCTION

Homogeneous nucleation is fundamental to forming liquid droplets or solid particles from the pure vapor. It plays an important role in atmospheric and industrial processes, such as the formation of clouds, droplets, rain and ice [1-3] and the synthesis of various nanomaterials [4,5]. To understand the nucleation process and obtain accurate nucleation rate, i.e., the number of nuclei formed in a unit volume per unit time [6], a large number of theoretical and experimental studies have been conducted for over a century [7]. The classical theoretical equation to calculate the nucleation rate is the Becker and Döring equation, also known as classical nucleation theory (CNT) [8]:

$$J_{CNT}=\sqrt{\frac{2\sigma}{\pi m_0}}v_0\left(\frac{p_v}{k_BT}\right)^2\exp\left(-\frac{16\pi v_0^2\sigma^3}{3(k_BT)^3(\ln S)^2}\right) \quad (1)$$

where S is the saturation ratio which is defined as the ratio of the vapor partial pressure (p_v) to the saturation pressure (p_s) corresponding to the given vapor temperature, that is $S=p_v/p_s$. Eq. (1) is based on thermodynamic equilibrium and the assumption that the micronucleus have well-defined macroscopic measurable quantities (equilibrium vapor pressure, surface tension and density) [9]. In addition, many experimental devices have been developed to study homogeneous nucleation, such as the expansion cloud chamber [10], shock tube [11], thermal diffusion cloud chamber [12], turbulent jet [13] and laminar flow diffusion chamber (LFDC) [14]. The latter is also called laminar flow aerosol generator, laminar flow reactor tube or laminar flow nucleation chamber. They all have almost the same operation principles. LFDC has been applied to measure the homogeneous nucleation rate with variable success from the 1970s [8,15]. In the LFDC, a particle free carrier gas first flows through a high temperature saturator and mixes with the saturated condensable vapor. Then the mixture is heated further to ensure no vapor condenses before it enters the wall-cooled tube. Once the mixture gets into the tube, a supersaturated zone is created at the center of the tube due to simultaneous heat and mass transfer; subsequently, a sharp nucleation peak is formed [14]. To avoid diffusion losses of the vapor and clusters on the tube wall as much as possible, it is favorable to use materials with the mass diffusivity smaller than the thermal diffusivity, or a large Lewis number (Le). Therefore, DBP is often used as a standard substance to study the homogeneous nucleation rate [9,16], because Le of DBP is much larger than unity for many kinds of carrier gases. For example, Le≈5.35 and 10.4 in argon and helium, respectively, under standard atmospheric conditions [17].

In some previous studies, the theoretical homogeneous nucleation rates of DBP did not agree well with the experimental data [18], due to not only the inherent flaws of theoretical equation stated

†To whom correspondence should be addressed.
E-mail: cjtsai@nctu.edu.tw

above, but also the improper calculation method of the nucleation rate. A conventional method to calculate the maximum experimental nucleation rate J_{exp}^{max} is based on the measured particle number concentration (N_p) at the outlet of the chamber [19]:

$$J_{exp}^{max} = fN_pQ_v \tag{2}$$

where f is the ratio of the maximum theoretical nucleation rate J_{theo}^{max} to the total theoretical droplet number per unit time, $\int J_{theo}dV$, which is calculated as:

$$f = \frac{J_{theo}^{max}}{\int J_{theo}dV} \tag{3}$$

It is obvious that J_{exp}^{max} calculated by Eq. (2) does not take into account the decrease of N_p due to droplet coagulation and deposition losses in the LFDC. This is speculated to be the reason why the experimental nucleation rate in [20] calculated by Eq. (2) does not agree well with the theoretical value calculated by Eq. (1). The former was 3 to 5 orders of magnitude larger than the theoretical value. To account for a more complete description of the nucleation process, computational fluid dynamics has been used for numerical study of this process. For example, a public package AeroSolved [21] was developed by Frederix et al. [22] based on the formation and transport of a single species of aerosol in an LFDC and whose study indicated the stability and accuracy of numerical solutions. The simulation results showed agreement with the experimental data in terms of the temperature profile at the centreline and average droplet number concentration at the outlet of the LFDC [22]. However, detailed droplet dynamic, transport mechanisms, such as different nucleation rate, droplet coagulation, vapor and droplet deposition losses were not included, these will be considered and discussed in this study.

The nucleation rate using the CNT cannot predict correctly the Gibbs free energy change associated with the formation of small clusters from the monomer vapor; Girshick and Chiu [23] proposed a self-consistent correction nucleation theory (SCCNT) to calculate the nucleation rate. The theoretical nucleation rates predicted by the SCCNT are in good agreement with the experimental results in many previous experimental and numerical studies. For example, the nucleation rates calculated using the SCCNT agrees well with reported data on the onset of nucleation for the SiH_4/H_2 and SiH_2Cl_2/H_2 systems [24]. Based on the nucleation rates calculated using the SCCNT, the simulated particle size distribution of silicon nanoparticles formed from the pyrolysis of monosilane agreed well with the experimental value [25]. Recently, an Eulerian large-eddy simulation was used to solve the PBE for DBP nucleation in turbulent flows using the SCCNT. The results showed reasonable agreement of predicted droplet number density with experimental data along the centreline of the LFDC [26]. It can be seen that the nucleation rate using the SCCNT was more suitable than that using the CNT in many previous simulation studies, so it was adopted and validated in this studies.

Coagulation plays an important role in the evolution of the droplet size distribution (DSD) during the transport process. However, it was often neglected in many previous theoretical studies and numerical simulations [22,25]. Recently, droplet coagulation was considered in the simulation of the rapid cooling of alcohol vapor. Results showed that coagulation is one of the dominant mechanisms in the DSD evolution after nucleation [27]. In addition, the mass loss due to vapor and droplet deposition on the wall was shown to be significant in Nguyen et al. [18], who pointed out the total mass loss of DBP was so high as 79.3% during the homogeneous nucleation and transport process in the LFDC. Neglecting these losses in the simulation led to the overestimation of the droplet number concentration [22]. Therefore, the mass loss of both vapor and droplet deposition was considered in this simulation.

The aim of this paper is (1) to improve the existing numerical model [22] for predicting the DSD of DBP in a LFDC. In the improved model, the SCCNT nucleation model was adopted, and droplet coagulation, vapor and droplet deposition losses were considered; (2) to validate the simulated DSD with the experimental values [18] and average number concentration with previous simulation results [22], respectively; and (3) to predict the number of molecules in the critical cluster calculated using the first nucleation theorem and compare that with the theoretical values.

NUMERICAL MODEL

In this section, the governing equations are introduced for solving the velocity, temperature and concentration profiles in the LFDC. These equations are discretized using proper discretization schemes.

1. Governing Equations

A one-way coupling Euler-Euler method is used to describe the homogeneous nucleation process of DBP in the LFDC. In the Euler-Euler framework, both the fluid and droplets are considered as continuous phase. The droplets are so small that they are assumed to follow the flow precisely with the same velocity. It is reasonable that the current system is a dilute system since the volume fraction of the droplets is only about 1.9×10^{-4} of the total volume as given in Section 3.2. In this study, the mixture temperature drops rapidly near the hot-cold zone interface, so a compressible formulation is required due to the strong dependence of the mixture properties on temperature [22]. The governing equations of the mixture model for the conservation of mass, momentum and energy are as follows:

$$\frac{\partial \rho}{\partial t} + \frac{\partial (\rho u_i)}{\partial x_i} = 0 \tag{4}$$

$$\frac{\partial \rho u_i}{\partial t} + \frac{\partial (\rho u_i u_j)}{\partial x_j} = -\frac{\partial p}{\partial x_i} + \frac{\partial}{\partial x_j}\left[\mu\left(\frac{\partial u_i}{\partial u_j} + \frac{\partial u_j}{\partial x_i} - \frac{2}{3}\frac{\partial u_k}{\partial x_k}\delta_{ij}\right)\right] \tag{5}$$

$$\frac{\partial (\rho c_p T)}{\partial t} + \frac{\partial (\rho c_p T u_j)}{\partial x_j} = \frac{\partial}{\partial x_j}\left(k_c\frac{\partial T}{\partial x_j}\right) + S_h \tag{6}$$

In these equations, the mixture properties are assumed mass fraction-weighted: $\rho=\Sigma Y_i\rho_i$, $\mu=\Sigma Y_i\mu_i$, $c_p=\Sigma Y_i c_{p,i}$ and $k_c=\Sigma Y_i k_{c,i}$ with ρ_i, μ_i, $c_{p,i}$ and $k_{c,i}$ being the corresponding density, viscosity, specific heat and thermal conductivity, respectively, Y_i is the mass fraction of the *i*th phase; here the phases are carrier gas, vapor and droplets, respectively. Y_c is defined as the ratio of the mass concentration of the vapor (m_c) to the total mass concentration of the mixture (m) in the tube [28,29]. The definitions of Y_v and Y_d are similar to that of Y_c, and they are given as: $Y_c=\frac{m_c}{m}$, $T_v=\frac{m_v}{m}$ and $Y_d=\frac{m_d}{m}$.

The sum of the mass fractions is equal to unity, or $Y_c+Y_v+Y_d=1$. For each phase, the mass conservation Equation (Eq. (4)) is as follows:

$$\frac{\partial \rho Y_c}{\partial t}+\frac{\partial(\rho Y_c u_i)}{\partial x_i}=\frac{\partial}{\partial x_i}\left(D\frac{\partial Y_c}{\partial x_i}\right) \tag{7a}$$

$$\frac{\partial \rho Y_v}{\partial t}+\frac{\partial(\rho Y_v u_i)}{\partial x_i}=\frac{\partial}{\partial x_i}\left(D\frac{\partial Y_v}{\partial x_i}\right)-S_{v\to d} \tag{7b}$$

$$\frac{\partial \rho Y_d}{\partial t}+\frac{\partial(\rho Y_d u_i)}{\partial x_i}=S_{v\to d} \tag{7c}$$

where $S_{v\to d}$ is the mass source term from the vapor to the droplet which is contributed by the nucleation (S_n) and growth (S_g) processes, and can be calculated as [24,27]:

$$S_{v\to d}=S_n+S_g \tag{8a}$$

$$S_n=\rho_d\left(\frac{1}{6}\pi d^{*3}\right)J_n \tag{8b}$$

$$S_g=2\pi\bar{d}\exp(-\ln^2\sigma_g)D\rho(1-Y_d)\ln\left(\frac{1-Y_v}{1-Y_{v,s}}\right)n(v,t) \tag{8c}$$

where $Y_{v,s}$ is saturated vapor mass fraction and expressed by the ideal gas law and Dalton's law [28]:

$$\frac{p_s}{k_BT}=\frac{\rho Y_{v,s}}{m_0} \tag{9}$$

where J_n is the nucleation rate which can be calculated by the CNT (Eq. (1)) and the SCCNT, J_{SCCNT} is given as [20,30]:

$$J_{SCCNT}=\sqrt{\frac{2\sigma}{\pi m_0}}v_0\left(\frac{p_v}{k_BT}\right)^2\left(\frac{e^{\theta}}{S}\right)\exp\left(-\frac{16\pi v_0^2\sigma^3}{3(k_BT)^3(\ln S)^2}\right) \tag{10}$$

where θ is the reduced macroscopic surface tension and calculated as $\theta=\sigma s_0/(k_BT)$, and $s_0=(36\pi v_0^2)^{1/3}$ is the surface area of a monomer. J_n calculated by the SCCNT (Eq. (10)) differs from that by the CNT (Eq. (1)) by a factor e^{θ}/S only, which the term e^{θ} comes from the change in the cluster free-energy expression and S^{-1} appears due to normalization in the kinetic theory [9,30]. d^* in Eq. (8b) is the diameter of the critical cluster and calculated by the Kelvin equation as [31]:

$$d^*=\frac{2\sigma v_0}{k_BT\ln S} \tag{11}$$

Then the theoretical number of molecules in the critical cluster, n^*, is calculated using d^* as $n^*=\frac{\pi d^{*3}}{6v_0}$. Combining Eq. (11), n^* can be calculated as

$$n^*=\frac{4\pi v_0^2\sigma^3}{3(k_BT\ln S)^3} \tag{12}$$

which is the so called Gibbs-Thomson equation.

In Eq. (8c), $\bar{d}$ is diameter of average mass and expressed in terms of droplet mass fraction Y_d and number concentration [26]:

$$\bar{d}=\left(\frac{6\rho Y_d}{\pi\rho_d n(v,t)}\right)^{1/3} \tag{13}$$

where n(v, t) is the continuous size distribution as a function of time t and droplet volume v, $v=(\pi d_d^3)/6$. It is governed by the general dynamics equation, or the so called population balance equation (PBE), which is expressed as:

$$\frac{\partial n(v,t)}{\partial t}+\frac{\partial[n(v,t)u_j]}{\partial x_j}+\frac{\partial[Gn(v,t)]}{\partial v}=J_n-J_c \tag{14}$$

On the left hand side of Eq. (14), the first term describes the change of the droplet number concentration with time, the second term is the change due to advection by the carrier gas, and the third term is the change due to droplet growth. On the right hand side, the first term represents the number of droplet produced by homogeneous nucleation, while the second term describes the change due to droplet coagulation, where the coagulation rate is calculated by [32,33]:

$$J_c=\frac{1}{2}\int_0^v\beta(v',v-v')n(v',t)n(v-v',t)dv' - n(v,t)\int_0^{\infty}\beta(v,v')n(v',t)dv' \tag{15}$$

where $\beta(v, v')$ is the collision kernel, which depends on the flow regions determined by Kn. In the continuum regime (Kn<0.1),

$$\beta(v,v')=K(v^{1/3}+v'^{1/3})\left(\frac{1}{v^{1/3}}+\frac{1}{v'^{1/3}}\right) \tag{16a}$$

where $K=2k_BT/3\mu$. In the slip flow regime (0.1<Kn<1),

$$\beta(v,v')=K(v^{1/3}+v'^{1/3})\left(\frac{C(v)}{v^{1/3}}+\frac{C(v')}{v'^{1/3}}\right) \tag{16b}$$

where C is the slip correction factor, C=1+1.246Kn. In the free molecular regime (Kn>10),

$$\beta(v,v')=\tilde{K}(v^{1/3}+v'^{1/3})\left(\frac{1}{v}+\frac{1}{v'}\right)^{1/2} \tag{16c}$$

where $\tilde{K}=\left[3\left(\frac{3}{4\pi}\right)^{1/16}\right]\left(\frac{\mu}{\rho}K\right)^{1/2}$.

The PBE (Eq. (14)) is coupled to governing equations Eqs. (4)-(6) via the velocity and mass source terms. To solve the PBE, the sectional method was employed [34]. In the sectional formulation of droplet size distribution, a finite sized domain is discretized into

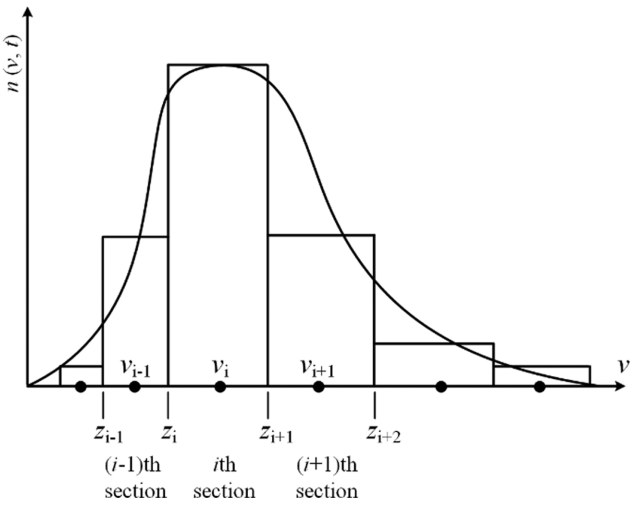

Fig. 1. A discretized size domain of droplet size distribution.

I arbitrarily sized adjacent intervals, as shown in Fig. 1. v_i is the representative size at the ith section (with $0 \le i \le I-1$) with $z_i < v_i < z_{i+1}$, in which z_i is the size at the sectional interface position between the (i-1)th and the ith section. Each section contains a representative size v_i allocated to all droplets. This enables the size distribution to be written as a finite sum of Dirac delta functions as:

$$n(v, t) = \Sigma_i N_i \delta(v - v_i) dv \tag{17}$$

where N_i is the total number of droplets per unit of volume or the zeroth moment of the size distribution in the ith section:

$$N_i = \int_{z_i}^{z_{i+1}} n(v, t) dv \tag{18}$$

Rather than solving the PBE (Eq. (14)) in terms of n(v, t), N_i is solved by taking the integral over the internal $[z_i, z_{i+1}]$ of the PBE with respect to v over each section. Here M_i is introduced to replace N_i and defined as $M_i = N_i/\rho$ It will be much more convenient numerically. Then the PBE takes the following form:

$$\frac{\partial \rho M_i}{\partial t} + \frac{\partial (\rho u_j M_i)}{\partial x_j} + \frac{\partial (\rho G M_i)}{\partial v} = J_{n,i} - J_{c,i} \tag{19}$$

where $J_{n,i} = \int_{z_i}^{z_{i+1}} J_n dv$ and $J_{c,i} = \int_{z_i}^{z_{i+1}} J_c dv$. Both represent the integral of nucleation and coagulation terms over the internal $[z_i, z_{i+1}]$.

2. Numerical Schemes

The open source CFD software package OpenFOAM® was used in the present simulation [35]. OpenFOAM provides a cell-centered collocated finite volume framework that can be used to solve the system of equations. In the finite volume method, Eq. (19) is integrated over a computational volume V with faces F as

$$\frac{\partial \rho M_i}{\partial t} + D(\phi_f M_{i,f}) + \rho G_{i+1} M_{i+1} - \rho G_i M_i = J_{n,i} - J_{c,i} \tag{20}$$

with the convective flux ϕ_f as

$$\phi_f = (\rho u)_f \cdot A_f \tag{21}$$

where $N_{i,f}$ represents the interpolation to the face f. The D-function denotes the discrete counterpart of the divergence term as a function of the specified flux, and defined as $D(\phi_f M_{i,f}) = \frac{1}{V} \Sigma_{f \in F} \phi_f M_{i,f}$. Using the implicit Euler scheme, Eq. (20) may be integrated from time tm at time m to $t^{m+1} = t^m + \Delta t$ at time m+1, as:

$$\begin{aligned} \frac{(\rho M_i)^{m+1} - (\rho M_i)^m}{\Delta t} &= -D(\phi_f M_{i,f})^{m+1} \\ &- \rho^{m+1} G_{i+1}^{m+1} M_{i+1}^{m+1} + \rho^m G_{i+1}^m M_{i+1}^m + J_{n,i}^{m+1} - J_{c,i}^{m+1} \end{aligned} \tag{22}$$

This equation can be solved using a modified PISO algorithm by means of an implicit predictor step and a number of corrector steps [22], the flow chart is shown in Fig. 2.

To solve Eqs. (4)-(6) and (20), the temporal, divergence, gradient and Laplacian terms were discretized separately in the OpenFOAM using proper discretization schemes. The time derivative term (ddtShemes) used an Euler transient scheme for discretization for transient simulations, Euler denotes a first-order implicit, bounded scheme. The gradient term (gradSchemes) used a Gaussian linear scheme; when the Gauss discretization is chosen, the gradient of the cell is obtained by Gauss's theorem which converts the volume integral into surface integral. These face values are then calculated using the cell center values with linear interpolation. The convective term (divSchemes) used Gauss linearUpwind linear scheme for U and T discretization, Gauss upwind scheme for V, Gauss linear scheme for Y and p. Though upwind scheme used here was only the first-order accurate, it was considered to be more appropriate due to its boundedness characteristics. The diffusive term (laplacianSchemes) used Gauss linear corrected scheme. The corrected expresses the surface normal gradient scheme and indicates an unbounded and second-order numerical behavior. For gradient term, convection term and diffusive term, in order to convert the cell center to the face center, an interpolation scheme (interpolationSchemes) was set to default linear. The surface normal gradient (snGradSchemes) used an uncorrected scheme for discretization [36]. The used standard schemes from OpenFOAM in this study

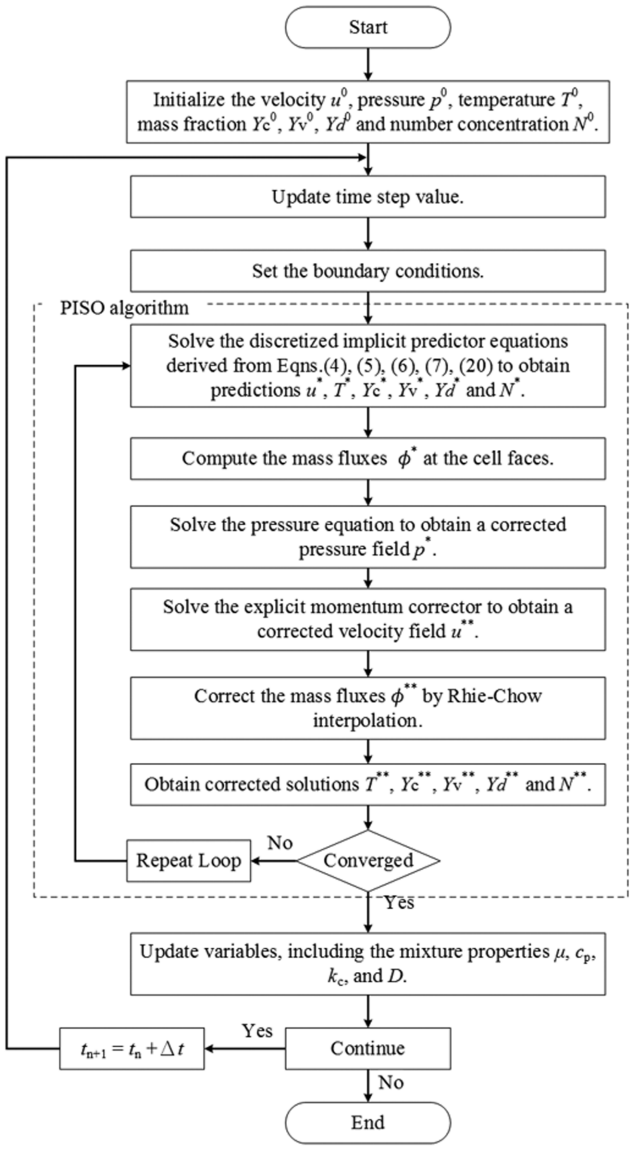

Fig. 2. The modified PISO algorithm.

Table 1. The standard schemes used from OpenFOAM in this study

Modeling term	Keywords for Scheme	Description	Scheme
Time derivative	*ddtShemes*	Discretization of the first time derivative	Euler
Gradient term	*gradSchemes*	Discretization of the gradient terms with an operator ∇	Gauss linear
Convection term	*divSchemes*	Discretization of the divergence terms with an operator ∇	Upwind
Diffusive term	*laplacianSchemes*	Discretization of the terms with the laplacian operator ∇^2	Gauss linearcorrected
Others	*interpolationSchemes*	Cell to face interpolations of the values	Linear
	snGradSchemes	Component of the gradient normal to a cell face	Corrected

are summarized in Table 1.

The transient state solution was used in the numerical studies with a time step of 10^{-4} second. The convergence criterion for the residual correctors was set to 10^{-6} for u, Y_c, Y_v, Y_d, T, and 10^{-7} for p. The mass imbalance value was assigned as 10^{-4} to ensure convergence.

PHYSICAL MODEL AND MATERIALS

1. Geometry of the LFDC

This numerical study was validated using the experimental data [18] in terms of the measured temperature profiles at the centerline, DSD and average number concentration at the outlet. The schematic diagram of the LFDC used in the experiment and the droplet formation, evolution and transport processes in the LFDC is shown in Fig. 3. The LFDC consists of two temperature zones separated by a hot-cold zone interface, which the hot zone is the preheater and the cold zone is the condenser. The radius of the tube is R=0.005 m, the lengths of the preheater and condenser are L_p=0.1 m and L_c=0.65 m, respectively. The temperatures at the inlet, walls of preheater and condenser are T_{in}=375.15 K, T_p=375.15 K and T_c=294.55 K, respectively. The flow rate is Q_v=1.0 L/min. Before the preheater, there is an additional tube long enough for the flow to become fully developed.

2. Boundary Conditions

The inlet velocity distribution (U_{in}) in the x-direction is parabolic as follows:

$$U_{in}=2\overline{U}\left[1-\left(\frac{r}{R}\right)^2\right] \tag{23}$$

The calculated Reynolds number is 46, which indicates that the flow is laminar. To calculate the vapor and droplet deposition losses, the trapped-type wall boundary condition was set. So the wall boundary condition is assumed as Dirichlet-type, i.e., a prefect sink for vapor and droplets, or Y_v=0 and Y_d=0 at the wall. This is different from that in Frederix et al. [22], which is Neumann-type or $\partial Y_v/\partial y$=0 and $\partial Y_d/\partial y$=0. Based on this assumption, the possibility of heterogeneous nucleation on the wall is neglected. All the boundary conditions including the velocity, pressure, temperature, mass fraction of carrier gas, vapor and droplet, and droplet concentration are listed in Table 2, where p_0 is the atmospheric pressure and set as p_0=101.325 pa, the inlet vapor is considered as a perfectly

Table 2. The boundary conditions

	Inlet	Outlet	Wall
Velocity	$u=U_{in}$	$\frac{\partial u}{\partial x}=0$	u=0
Pressure	$\frac{\partial p}{\partial x}=0$	$p=p_0-\frac{1}{2}\rho\lvert u\rvert^2$	$\frac{\partial p}{\partial y}=0$
Temperature	$T=T_{in}$	$\frac{\partial T}{\partial x}=0$	$T=T_{wall}$
Vapor mass fraction	$Y_v=Y_{in}$	$\frac{\partial Y_v}{\partial x}=0$	$Y_v=0$
Carrier gas mass fraction	$Y_c=1-Y_{in}$	$\frac{\partial Y_c}{\partial x}=0$	$\frac{\partial Y_c}{\partial y}=0$
Droplet mass fraction	$Y_d=0$	$\frac{\partial Y_d}{\partial x}=0$	$Y_d=0$
Droplet concentration	n(0, t)=0	$\frac{\partial n(v,t)}{\partial x}=0$	n(v, t)=0

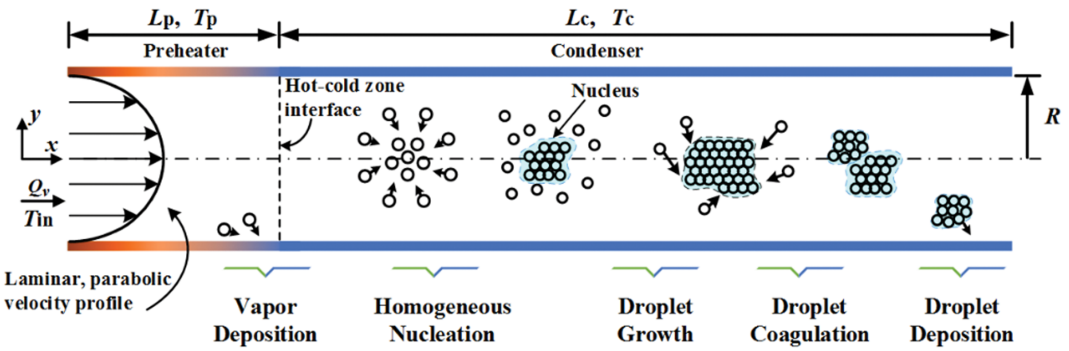

Fig. 3. The schematic diagram of the LFDC used in the experiment and the droplet formation, evolution and transport processes in the LFDC.

Table 3. The physiochemical properties of DBP

Quantity	Formula	References
ρ_d	$1047.0-0.81758(T-293.15)$	[26]
σ	$36.399-0.08713(T-273)$	[26]
p_s	$133.3\exp\left(16.27-\frac{5099}{T-109.5}\right)$	[18]
D	$0.03442(T^{1.927}/273.17)$	[41]

saturated flow at the inlet temperature (T_{in}), then the initial condition for Y_v is set as $Y_{in}=r(t)Y_{v,s}(T_{in})$, where r(t) is a ramping function [22], $Y_{v,s}(T_{in})$ is calculated by Eq. (9) at temperature T_{in}, so the initial condition $Y_{in}\approx1.8\times10^{-4}$ and the maximum mass fraction of droplets is also 1.8×10^{-4} according to mass conservation in the phase transformation process; the corresponding maximum volume fraction of droplets is about 1.9×10^{-4}.

3. Physiochemical Properties of DBP

The nucleation rate is affected by the physiochemical properties of DBP [9], such as the saturation pressure and the diffusion coefficient of the vapor phase, the density and the surface tension of the liquid phase, which are influenced by temperature. The equations used to calculate the physiochemical properties were selected from the literature and listed in Table 3 with the reasons stated in the Supplementary Materials.

RESULTS AND DISCUSSION

1. Model Validation

The mesh density is one of the key factors that determines the accuracy of the numerical simulation. A two-dimensional wedge-shaped geometry and structural meshes were used in this study. Four different mesh densities with different numbers of cells N_x and N_y, and the corresponding cell sizes of Δx and Δy in x and y directions were tested, namely, coarse, medium, fine and very fine, respectively, and the values are listed in Table 4.

The DSD was selected to evaluate the effect of the mesh density on the simulated results, which was assumed to follow the log-normal size distribution as [33]:

$$n(v,t)=\frac{N(t)}{3\sqrt{2\pi}\ln\sigma_g(t)}\exp\left(-\frac{\ln^2(v/v_g(t))}{18\ln^2(\sigma_g(t))}\right)\frac{1}{v} \tag{24}$$

where N(t) is the total number concentration of droplets, $v_g(t)$ is the geometric mean volume and $v_g=(\pi d_g^3)/6$, d_g is the geometric mean diameter which equals to the count median diameter (CMD) for the lognormal number distribution. The CMD is converted from the diameter of the average droplet mass $\bar{d}$ in Eq. (13), using

Table 4. The values of N_x, N_y, Δx and Δy

	N_x	N_y	Δx	Δy
Coarse (480 cells)	60	8	0.0125 m	0.000625 m
Medium (1,536 cells)	96	16	0.0078 m	0.000313 m
Fine (3,072 cells)	192	16	0.0039 m	0.000313 m
Very fine (16,384 cells)	512	32	0.0015 m	0.000156 m

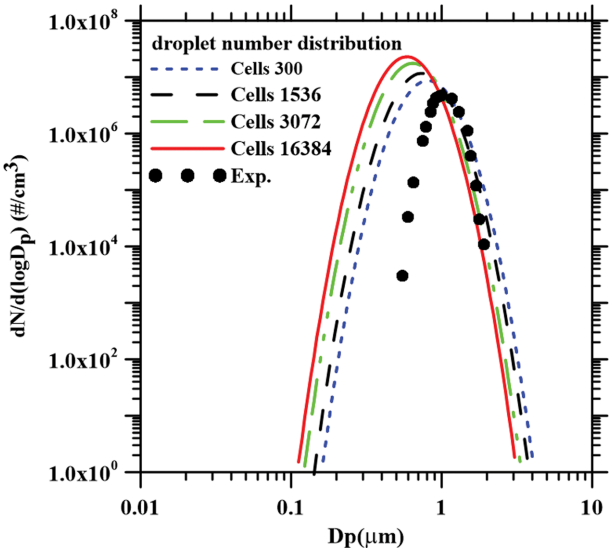

Fig. 4. The effect of the mesh density on the DSD at the outlet of the LFDC.

the Hatch - Choate equation as follows [31]:

$$CMD=\bar{d}/\exp(1.5\ln^2\sigma_g) \tag{25}$$

Fig. 4 shows the effect of the mesh density on the DSDs at the outlet of the LFDC. The results indicated that the DSDs calculated from the coarse and medium meshes deviated from the fine and very fine meshes significantly, while the latter two generated similar results. Therefore, 3,072 cells were used in the subsequent simulations with considering the computational cost.

In the simulation, a correct temperature profile is the prerequisite to obtain a correct nucleation rate. The numerical temperature profiles versus the experimental values at the wall and axis positions, respectively, are shown in Fig. 5(a). Wall temperature stays uniform within the first 0.05 m after the inlet and starts to drop rapidly from 375.15 K to 294.55 K near the hot-cold zone interface. The maximum difference between the present simulation and experiment results [18] is 2%. For the axial temperature, the numerical results are slightly higher than the experimental values in the preheater due to experimental uncertainties. In general, the simulated temperature profiles can be regarded as reasonable. The vapor partial pressure, saturation pressure and saturation ratio at the axis of the LFDC are shown in Fig. 5(b). It shows that the partial pressure decreases rapidly with decreasing temperature near the hot-cold zone interface, which results in the saturation ratio rises steeply and droplet nucleation will ensue.

2. Nucleation Rate

The numerical nucleation rates along the axial position without considering droplet coagulation and deposition loss are shown in Fig. 6. At the beginning, no clusters of liquid phase are formed since the nucleation rate calculated by Eq. (10) is only valid for $S\geq1$, meaning supersaturation. After $S\geq1$, clusters are formed in the supersaturated vapor due to fluctuations; however, the clusters are subcritical sizes at first, they are unstable and trend to get reduced. When the clusters are supercritical, they are stable and grow to macroscopic sizes. So there is a certain critical value S_c, for stable

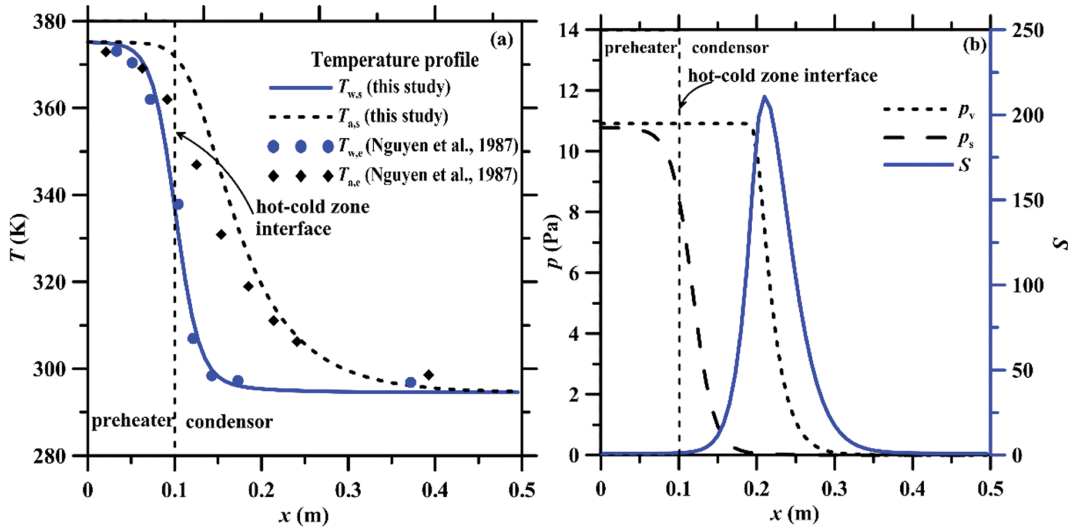

Fig. 5. (a) Temperature profiles at the axis (T_a) and wall (T_w) of the LFDC. (b) The vapor partial pressure (p_v), saturation pressure (p_s) and saturation ratio (S) at the axis of the LFDC. Q_v=1.0 L/min, T_p=375.15 K and T_c=294.55 K.

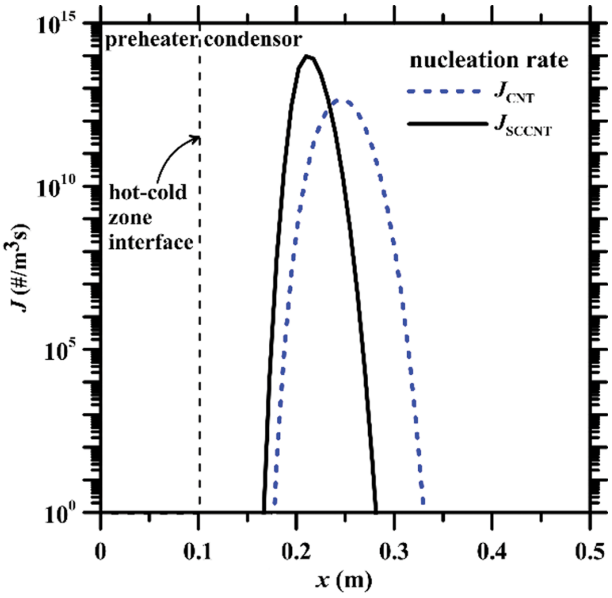

Fig. 6. The numerical nucleation rates along the axial position without considering droplet coagulation and deposition loss.

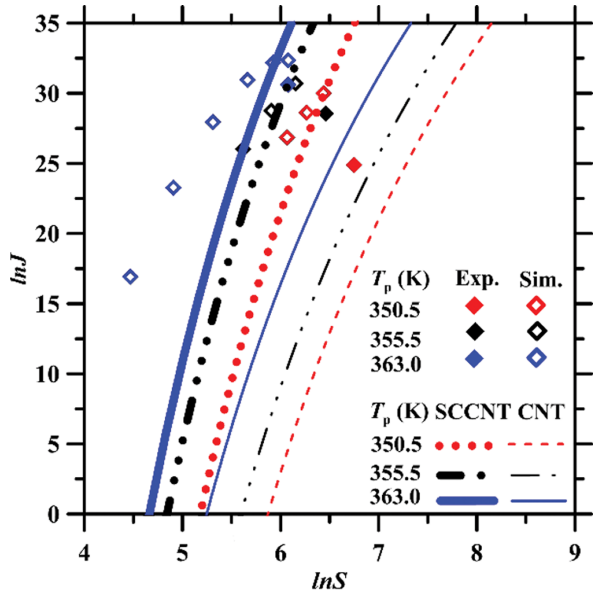

Fig. 7. The comparison of theoretical and simulated nucleation rates with experimental results [18] at different temperatures (T_p).

formation, S_{cr}=7.11 at L_x=0.14 m for SCCNT and S_{cr}=11.44 at L_x=0.15 m for CNT, respectively, in this study. That is the nucleation predicted by the SCCNT occurs earlier than by the CNT. The reason is that J_{SCCNT} is larger than J_{CNT} at a lower S by the factor e^{θ}/S. With the nucleation rate increasing steeply, the nucleation peaks at L_x=0.21 m predicted by the SCCNT appear also earlier than that at L_x=0.25 m predicted by the CNT, and the value of the nucleation peak is 9.6×10^7 #/cm^{3}s calculated by the SCCNT which is higher than 4.6×10^6 #/ cm^{3}s calculated by the CNT. Similar results for the magnitude of nucleation peaks have been observed by Hämeri and Kulmala [15]. After cluster formation, consequent condensation growth will continue on the formed clusters. When $(\ln S)^{-2}$ goes to infinitesimal for S→1, the exponent term in Eq. (10) becomes zero once the saturation drops below unity, so the nucleation stops effectively.

Fig. 7 shows the comparison of the theoretical and simulated homogeneous nucleation rates with the experimental results at different preheater temperatures (T_p) of 363.0 K, 355.5 K and 350.5 K which were calculated by Eq. (2) using the measured droplet number concentration at the LFDC outlet [18].

Compared with the experimental values, the CNT underestimates the nucleation rate up to six orders of magnitude. In comparison, the SCCNT overestimates the nucleation rate by only up to two orders of magnitude, which is a significant improvement. That is, the SSCNT is more suitable to calculate the nucleation rate than the CNT. It can also be seen that the slopes of lnJ versus lnS

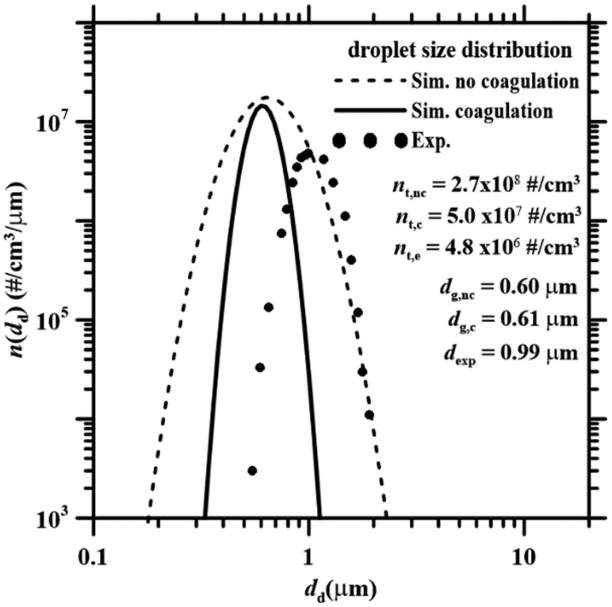

Fig. 8. The comparison of DSDs at the outlet of the LFDC with and without considering droplet coagulation with experimental results [18].

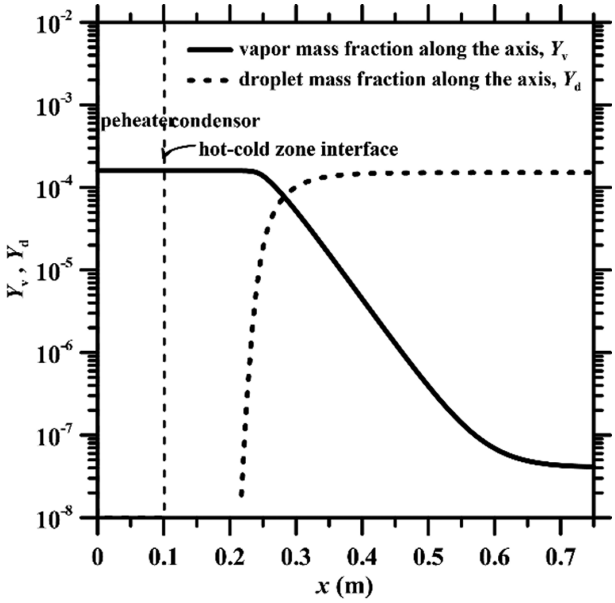

Fig. 9. The vapor and droplet mass fractions along the axis.

calculated by both CNT and SCCNT are near constant, which contain the information of the critical cluster size and will be discussed in the last section.

3. Droplet Size Distribution

The droplet size distribution and average number concentration at the outlet of the LFDC were measured in the experimental study [18] and used to validate the simulation results. The DSD is affected by both droplet coagulation and vapor and droplet deposition losses. First, only the role of droplet coagulation was considered, the simulated DSDs with and without considering droplet coagulation are shown in Fig. 8. With coagulation, d_g is 0.61 μm ($d_{g,c}$), which is a littler larger than 0.60 μm ($d_{g,nc}$) without coagulation. However, σ_g predicted with coagulation is 1.18 ($\sigma_{g,c}$), which is smaller than 1.34 ($\sigma_{g,nc}$) without coagulation. N_t is decreased significantly from 2.7×10^8 #/cm^3 ($N_{t,nc}$) to 5.0×10^7 #/cm^3 ($N_{t,c}$) when droplet coagulation is considered. It can be seen that droplet coagulation affects both the geometric standard deviation (σ_g) and the total number concentration (N_t) significantly.

Secondly, the effect of vapor and droplet deposition losses on the DSD was studied based on using the SCCNT and considering of droplet coagulation. The wall boundary condition was set as trapped-type. The numerical results of the mass fraction of the remaining vapor and droplets, Y_v and Y_d, respectively, along the axis are shown in Fig. 9.

Y_v stays at the level of 1.8×10^{-4} until L_x=0.25 m, then it starts to decrease slowly to 4.9×10^{-8} at L_x=0.65 m. Due to droplet nucleation peak at L_x=0.21 m as shown in Fig. 6, Y_d increases rapidly to 1.32×10^{-5} at L_x=0.33 m and thereafter becomes stable. The vapor is converted to droplets when S is larger than unity within the range of 0.15 to 0.33 m as shown in Fig. 5(b). It can be seen that Y_v at the inlet is 1.8×10^{-4}, which is much larger than the sum of Y_v and Y_d at the outlet, 1.32×10^{-5}. That is, the vapor and droplet losses are severe in the LFDC.

To calculate both vapor deposited on the wall from the inlet of the LFDC and droplets deposited after nucleation, the cumulative fractional deposition loss is used and expressed as:

$$f = 1 - \frac{Y_t(x)}{Y_t(0)} \tag{26}$$

where $Y_t(x)$, $Y_t(0)$ are the total mass fractions of vapor and droplets at position x and inlet (x=0), respectively. $Y_t(x) = \dfrac{\int_A [Y_v(x) + Y_d(x)]udA}{\int_A udA}$,

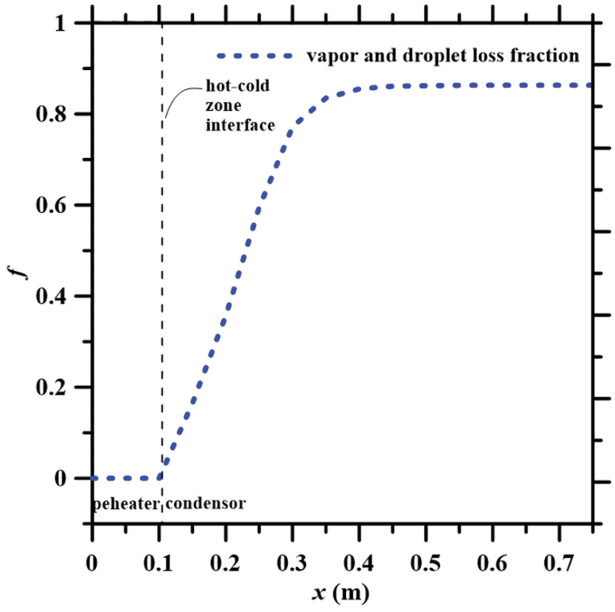

Fig. 10. The cumulative total fractional deposition loss in x-direction.

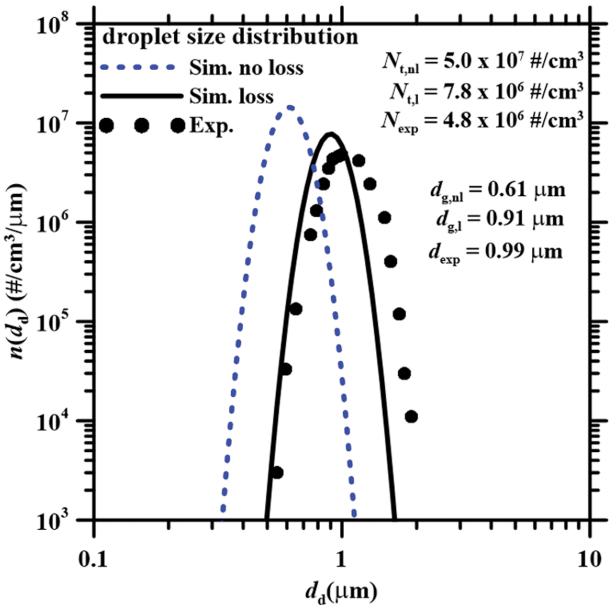

Fig. 11. The comparison of the simulated DSDs with and without vapor and droplet losses with experimental results [18].

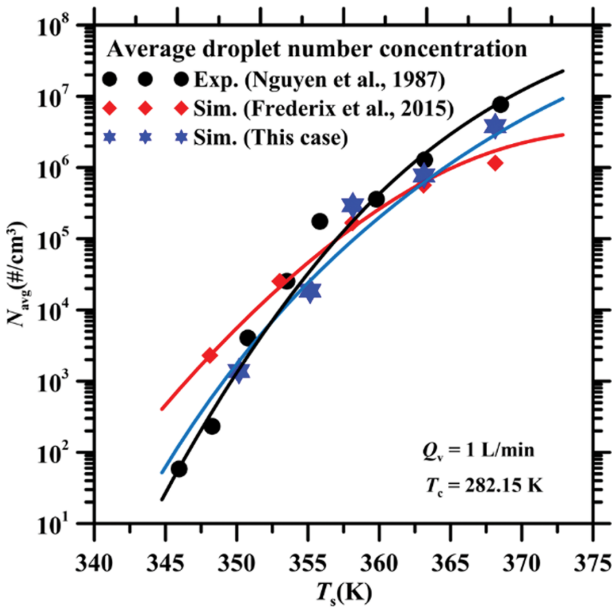

Fig. 12. The comparison of the simulated droplet number concentration at the outlet of LFDC with previous data [18] at a flow rate of 1.0 L/min, T_c=282.1 K and different preheater temperatures.

$$Y_t(0)=\frac{\int_A [Y_v(0)]udA}{\int_A udA}.$$

Fig. 10 displays the cumulative total fractional deposition loss in x-direction. The total fractional loss at the outlet is 86.3%, which is close to the experimental value of 79.3% [18]. To the best of our knowledge, this is the first time to consider the vapor and the droplet losses in the simulation, which helps to reduce the error between the simulated and experimental results. Actually, the deposition mechanism is complex, such as thermophoresis deposition may be existing in the tube flow due to the temperature difference between the centerline and wall as shown in Fig. 5(a) [37]. The deposition velocity increases with the increasing surface roughness, particularly for small sized materials [38]. These are not considered in this model.

Fig. 11 shows the comparison of the simulated DSDs with and without the consideration of vapor and droplet losses with experimental results [18]. Without loss, d_g is 0.61 μm ($d_{g,nl}$) which is much smaller than that with loss ($d_{g,l}$), 0.91 μm. The latter is closer to the experimental result of 0.99 μm (d_{exp}). The difference between the simulated diameter and experimental data is 8.08%. N_t is 5.0×10^7 #/cm^3 ($N_{t,nl}$) without considering loss, which is much higher than that with loss ($N_{t,l}$), 7.8×10^6 #/cm^3. The latter is closer to the experimental result of 4.8×10^6 #/cm^3 (N_{exp}). N_t of both simulation and experiment is within the same order of magnitude. It is obvious that DSDs are shifted towards larger diameters due to the vapor and droplet losses. That is, vapor and droplet losses affect the simulated DSDs significantly and need to be considered in the simulation.

Fig. 12 shows the comparison of the average droplet number concentration ($\overline{N}$) at the outlet of LFDC for this study, previous simulated results and experimental data. The simulations are performed on a flow rate of 1.0 L/min, T_c=282.1 K and T_p=368.0 K, 363.1 K, 358.1 K, 355.5 K, 350.5 K, respectively. $\overline{N}$ is calculated by the equation as follows:

$$\overline{N}=\frac{1}{A_{out}}\int_{A_{out}} n_{out}(v, t)dA \quad (27)$$

where A_{out} is the surface area and $n_{out}(v, t)$ is the number concentration at the outlet. The results show that $\overline{N}$ of both experiment and simulation increase with the increasing preheater temperature. The prediction of $\overline{N}$ by both this model and previous model is in reasonable agreement with the experimental data. But $\overline{N}$ predicted by this model is closer to the experimental data than that by previous model [18,22]. For the low T_s, here T_s<355 K, this model can reduce the overestimation by the previous model with a consideration of vapor and droplet deposition losses as shown in Fig. 11. For the high T_s, here T_s>355 K, this model can also improve the accuracy for predicting the number concentration compared to the previous model [22]. The reason may be that the large temperature difference at high T_s results in high saturation, and subsequent larger nucleation rate and formed droplets by the SCCNT using this model than that by the CNT using previous model.

From the comparison of the DSDs in Fig. 8 and Fig. 11, and average number concentration in Fig. 12 for without and with coagulation and deposition, it is clear that the droplet size and number concentration was not only affected by nucleation process, but also by coagulation and deposition.

4. Critical Cluster Size

Using the slopes of the isothermal curves of lnJ and lnS as shown in Fig. 7, the number of molecules in the critical cluster n_s can be calculated by the first nucleation theorem, the equation is as follows [39,40]:

$$n_s=\left(\frac{\partial \ln J}{\partial \ln S}\right)_T \quad (28)$$

The comparison of the predicted n_s was calculated by Eq. (28) at

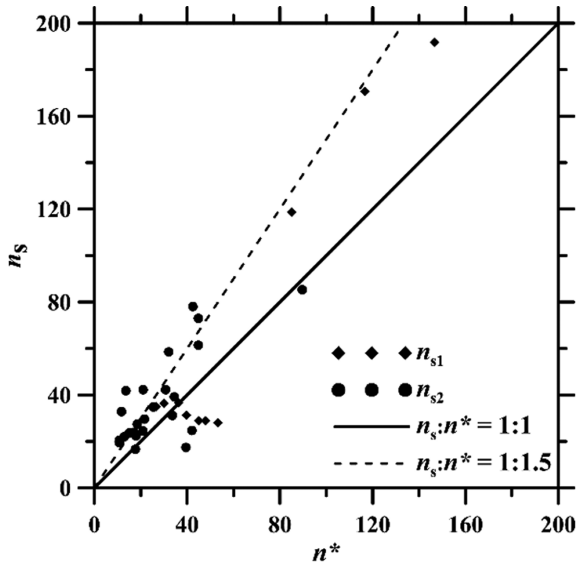

Fig. 13. The simulated number of molecules in the critical cluster, n_s, plotted against that predicted of the Gibbs-Thompson equation, n^*.

two different temperatures, T_p=363 K (n_{s1}) and 355 K (n_{s2}), respectively, with the theoretical n^* calculated by Eq. (12) shown in Fig. 13. It is seen that n_s is about 50% more than n^* in general, or the Gibbs-Thompson equation under-predicts the critical cluster size. However, when n_s is near 40, the n_s fluctuates around 1 : 1 line. The critical cluster size will be measured in future studies and used to validate the simulated results. This can be used to make a better understanding of the process of the droplet nucleation and formation.

CONCLUSION

Euler-Euler method was used in the OpenFOAM to study the homogeneous nucleation process of DBP in the LFDC. Suitable DBP physiochemical properties were selected and the effects of different nucleation models, droplet coagulation and deposition loss were considered. The numerical results indicated that the nucleation rate using the SCCNT explained the underestimation of that using the CNT when compared with the experimental values. The droplet coagulation process decreased the geometric standard deviation and the total number of generated droplets. The vapor and droplet deposition losses on the wall caused 86.3% mass loss and resulted in a shift of DSDs towards larger diameters. Based on these considerations the agreement between the simulated and experimental DSDs improved. The predicted number of molecules in the critical cluster calculated using the simulated nucleation rate and saturation ratio is about 50% more than that calculated by the Gibbs-Thompson equation. In the future, the droplet coagulation, vapor and droplet deposition losses should be considered in the simulation of the process of droplet formation, evolution and transport. To further reduce the discrepancy between simulation prediction and experimental data, a more detailed mechanism of droplet formation and transport should be considered, such as heterogeneous nucleation on the wall and thermophoresis deposition to the wall.

ACKNOWLEDGEMENT

The authors would like to express gratitude for the financial support of the Taiwan Ministry of Science and Technology via the contracts MOST 108-2622-8-009-012-TE5, 107-3011-F-009-002- and 107-2221-E-009-004-MY3, and the Higher Education Sprout Project of the National Chiao Tung University and Ministry of Education (MOE), Taiwan.

NOMENCLATURE

A : cross section area of the tube [m^2]
c_p : specific heat [J/K]
D : diffusion coefficient [cm^2/s]
k_B : Boltzmann constant [J/K]
k_c : thermal conductivity [W/(m·K)]
Kn : Knudsen number, Kn=$2\lambda/d_d$
m_0 : molecular mass [kg]
N_p : measured particle number concentration at the outlet [#/m^3]
p : pressure [pa]
p_s : saturation pressure [pa]
Q_v : flow rate [L/min]
S_h : production of enthalpy [J]
T : vapor temperature [K]
$\overline{U}$: average velocity in the tube [m/s]
v_0 : molecular volume [m^3]
δ_{ij} : Kronecker delta
λ : mean free path of the gas [m]
μ : viscosity [m^2/s]
ρ : mixture density [kg/m^3]
ρ_d : droplet density [kg/m^3]
σ : surface tension of the bulk vapor-liquid interface [mN/m]
σ_g : geometric standard deviation of the DSD

SUPPORTING INFORMATION

Additional information as noted in the text. This information is available via the Internet at http://www.springer.com/chemistry/journal/11814.

REFERENCES

1. D. Barahona and A. Nenes, *J. Geophys. Res.*, **113**, D11211 (2008).
2. Z. Han, X. Han, H. Li and P. Li, *Korean J. Chem. Eng.*, **333**, 487 (2016).
3. K. Mochizuki, Y. Qiu and V. Molinero, *J. Am. Chem. Soc.*, **139**, 17003 (2017).
4. R. Patakfalvi, S. Papp and I. Dékány, *J. Nanopart. Res.*, **9**, 353 (2007).
5. T. Ryu, M. Olivas-Martinez, H. Y. Sohn, Z. Z. Fang and T. A. Ring, *Chem. Eng. Sci.*, **65**, 1773 (2010).
6. Z. Kožíšek and P. Demo, *J. Aerosol Sci.*, **40**, 802 (2009).
7. B. E. Wyslouzil and J. Wölk, *J. Chem. Phys.*, **145**, 211702 (2016).
8. A. A. Manka, D. Brus, A. P. Hyvarinen, H. Lihavainen, J. Wölk and R. Strey, *J. Chem. Phys.*, **132**, 244505 (2010).
9. K. Hämeri and M. Kulmala, *J. Chem. Phys.*, **105**, 7696 (1996).
10. P. E. Wagner and R. Strey, *J. Phys. Chem.*, **85**, 2694 (1981).

11. K. N. H. Looijmans and M. E. H. Van Dongen, *Exp. Fluids*, **23**, 54 (1997).
12. D. Kane and M. S. El-Shall, *J. Chem. Phys.*, **105**, 7617 (1996).
13. T. K. Lesniewski and S. K. Friedlander, *P. Roy. Soc. A-Math. Phys.*, **454**, 2477 (1998).
14. H. Lihavainen, Y. Viisanen and M. Kulmala, *J. Chem. Phys.*, **114**, 10031 (2001).
15. M. P. Anisimov and A. G. Cherevko, *J. Aerosol Sci.*, **16**, 97 (1985).
16. K. Okuyama, Y. Kousaka, D. R. Warren, R. C. Flagan and J. H. Seinfeld, *Aerosol Sci. Technol.*, **6**, 15 (1987).
17. K. Hämeri, M. Kulmala, E. Krissinel' and G. Kodenyov, *J. Chem. Phys.*, **105**, 7683 (1996).
18. H. V. Nguyen, K. Okuyama, T. Mimura, Y. Kousaka, R. C. Flagan and J. H. Seinfeld, *J. Colloid Interface Sci.*, **119**, 491 (1987).
19. P. E. Wagner and M. P. Anisimov, *J. Aerosol Sci.*, **24**, S103 (1993).
20. M. P. Anisimov, K. Hämeri and M. Kulmala, *J. Aerosol Sci.*, **25**, 23 (1994).
21. AeroSolved, available at: https://www.intervals.science/resources/aerosolved, accessed on September 10th, 2019.
22. E. M. A. Frederix, M. Stanic, A. K. Kuczaj, M. Nordlund and B. J. Geurts, *Int. J. Multiphase Flow*, **74**, 184 (2015).
23. S. L. Girshick and C. P. Chiu, *J. Chem. Phys.*, **93**, 1273 (1990).
24. F. E. Kruis, J. Schoonman and B. Scarlett, *J. Aerosol Sci.*, **25**, 1291 (1994).
25. R. Körmer, H. J. Schmid and W. Peukert, *J. Aerosol Sci.*, **41**, 1008 (2010).
26. G. Neuber, A. Kronenburg, O. T. Stein and M. J. Cleary, *Chem. Eng. Sci.*, **167**, 204 (2017).
27. C. Winkelmann, A. K. Kuczaj, M. Nordlund and B. J. Geurts, *J. Eng. Math.*, **108**, 171 (2017).
28. C. Winkelmann, M. Nordlund, A. K. Kuczaj, S. Stolz and B. J. Geurts, *Int. J. Numer. Meth. Fluids*, **74**, 313 (2014).
29. S. Patankar, *Numerical heat transfer and fluid flow*, CRC press, New York (1980).
30. K. Mullick, A. Bhabhe, A. Manka, J. Wölk, R. Strey and B. E. Wyslouzil, *J. Phys. Chem. B*, **119**, 9009 (2015).
31. W. C. Hinds, *Aerosol technology: properties, behavior, and measurement of airborne particles*, Wiley, New York (1999).
32. K. W. Lee and H. Chen, *Aerosol Sci. Technol.*, **3**, 327 (1984).
33. J. S. Youn, S. Park, H. Cho, Y. W. Jung and K. J. Jeon, *Korean J. Chem. Eng.*, **35**, 1948 (2018).
34. E. M. A. Frederix, A. K. Kuczaj, M. Nordlund, A. E. P. Veldman and B. J. Geurts, *J. Aerosol Sci.*, **104**, 123 (2017).
35. OpenFOAM, available at: https://www.openfoam.com, accessed on September 10th, 2019.
36. V. H. Bhusare, M. K. Dhiman, D. V. Kalaga, S. Roy and J. B. Joshi, *Chem. Eng. J.*, **317**, 157 (2017).
37. J. S. Lin, C. J. Tsai and C. P. Chang, *J. Aerosol Sci.*, **35**, 1235 (2004).
38. W. Hong and X. Wang, *Korean J. Chem. Eng.*, **35**, 1517 (2018).
39. D. Kashchiev, *J. Chem. Phys.*, **76**, 5098 (1982).
40. G. G. Kodenev, A. V. Samodurov, M. N. Baldin and A. M. Baklanov, *Colloid J.*, **76**, 38 (2014).
41. M. Wilck, K. Hämeri, F. Stratmann and M. Kulmala, *J. Aerosol Sci.*, **29**, 899 (1998).

Supporting Information

A detailed numerical study on the evolution of droplet size distribution of dibutyl phthalate in a laminar flow diffusion chamber

Feng Jia*, Zi-Yi Li, David Y. H. Pui***,****, and Chuen-Jinn Tsai*,†**

*Institute of Environmental Engineering, National Chiao Tung University, Hsinchu 300, Taiwan
**School of Energy and Environmental Engineering, University of Science and Technology Beijing, Beijing 100083, China
***Mechanical Engineering Department, University of Minnesota, Minneapolis, MN 55455, USA
****School of Science and Engineering, The Chinese University of Hong Kong, Shenzhen, Guangdong 518172, China
(*Received 25 September 2019 • accepted 7 December 2019*)

Different equations in the literatures to predict the physicochemical properties of DBP were examined for the accuracy in this Supporting Materials. The equations of Hämeri et al. [2], AIChE [2], Frederix et al. [3] and Neuber et al. [4] were used to calculate the saturation pressure of DBP, and the equations of Fuller et al. [5], Bedanov et al. [6], Wilck et al. [7] and Frederix et al. [3] were used to predict the diffusion coefficient of DBP in air. All of these equations are summarized in Table S1. Calculated values using these equations were compared with the experimental data in the temperature range of 280 to 420 K for the saturation pressure of Neuber et al. [4] and the diffusion coefficient data of Lugg [8] and Davis and Chorbajian [9]. As can be seen from Fig. S1, the equations

Table S1. The saturation pressure and diffusion coefficient of DBP in open literatures

Quantity	Formula	References
Saturation pressure p_s (Pa)	$133.3\exp\left(16.27-\frac{5099}{T-109.5}\right)$	[1]
	$\exp\left(160.25-\frac{16941}{T}-19.254\ln T+\frac{6.63\times10^{-6}}{T^2}\right)$	[2]
	$2.1965\times10^{14}\exp(-1.1497\times10^{4}T^{-1})$	[3]
	$10^{-27.567+0.118T-0.000112T^2}$	[4]
Diffusion coefficient D (cm^2/s)	$0.25T^{1.75}/p$	[5]
	$0.0005T-0.1088$	[6]
	$0.03442(T^{1.927}/273.17)$	[7]
	$0.0398(T/273.16)^{1.5}$	[3]

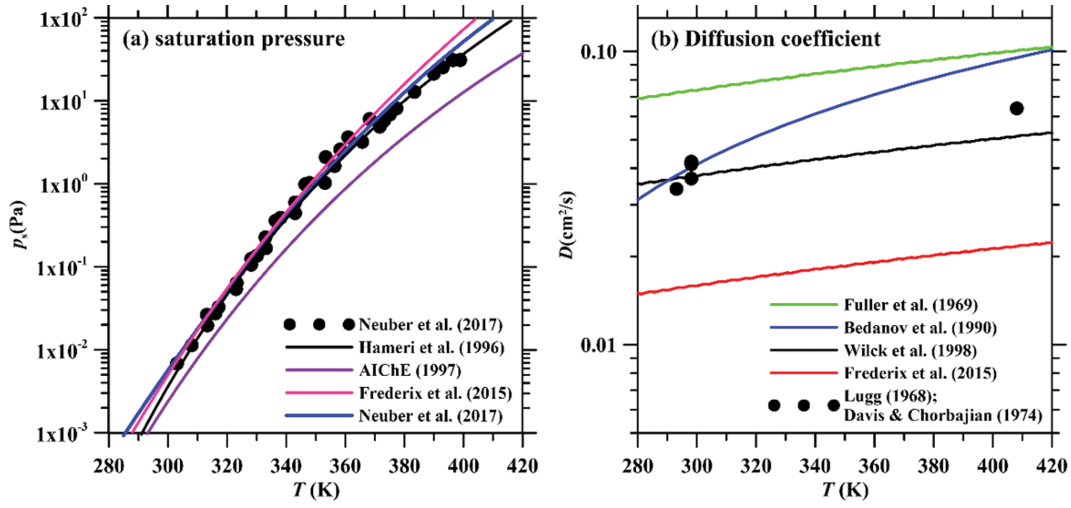

Fig. S1. Effect of temperature on (a) saturation pressure, (b) diffusion coefficient in the temperature range of 280 to 420 K.

given by Hämeri et al. [1] and Wilck et al. [7] agree well with the previous experimental data and therefore are used in the present simulation model.

REFERENCES

1. K. Hämeri, M. Kulmala, E. Krissinel' and G. Kodenyov, *J. Chem. Phys.*, **105**, 7683 (1996).
2. AIChE DIPPR (Design Institute for Physical Property Data) Thermodynamical Database, American Institute of Chemical Engineers, New York (1997).
3. E. M. A. Frederix, M. Stanic, A. K. Kuczaj, M. Nordlund and B. J. Geurts, *Int. J. Multiphas. Flow*, **74**, 184 (2015).
4. G. Neuber, A. Kronenburg, O. T. Stein and M. J. Cleary, *Chem. Eng. Sci.*, **167**, 204 (2017).
5. E. N. Fuller, K. Ensley and J. C. Giddings, *J. Phys. Chem.*, **73**, 3679 (1969).
6. V. M. Bedanov, V. S. Vaganov, G. V. Gadiyak, G. G. Kodenev and A. Rubakhin, *Sov. J. Chem. Phys.*, **7**, 917 (1990).
7. M. Wilck, K. Hämeri, F. Stratmann and M. Kulmala, *J. Aerosol Sci.*, **29**, 899 (1998).
8. G. A. Lugg, *Anal. Chem.*, **40**, 1072 (1968).
9. E. J. Davis and E. Chorbajian, *Ind. Eng. Chem. Fundam.*, **13**, 272 (1974).